Dual Polyanion Mechanism for Superionic Transport in BH$_4$-Based Argyrodites

Pengbo Wang, Haoyu Liu, Sawankumar Patel, Jason E. Roberts, Yudan Chen, Bright Ogbolu, Brian E. Francisco,* and Yan-Yan Hu*

Polyanion rotations are often linked to cation diffusion, but the study of multiple polyanion systems is scarce due to the complexities in experimentally determining their dynamic interactions. This work focuses on BH$_4$-based argyrodites, synthesized to achieve a high conductivity of 11 mS cm^{-1}. Advanced tools, including high-resolution X-ray diffraction, neutron pair distribution function analysis, and mutinuclear magic-angle-spinning nuclear magnetic resonance (NMR) spectroscopy and relaxometry, along with theoretical calculations, are employed to unravel the dynamic intricacies among the dual polyanion lattice and active charge carriers. The findings reveal that the anion sublattice of Li$_{5.07}$PS$_{4.07}$(BH$_4$)$_{1.93}$ affords an even temporal distribution of Li among PS$_4^{3-}$ and BH$_4^-$, suggesting minimal trapping of the charge carriers. Moreover, the NMR relaxometry unveils rapid BH$_4^-$ rotation on the order of ~GHz, affecting the slower rotation of neighboring PS$_4^{3-}$ at ~100 MHz. The PS$_4^{3-}$ rotation synchronizes with Li$^+$ motion and drives superionic transport. Thus, the PS$_4^{3-}$ and BH$_4^-$ polyanions act as two-staged dual motors, facilitating rapid Li$^+$ diffusion.

1. Introduction

Next-generation rechargeable batteries require electrolytes with high ionic conductivities and low mass densities for enhanced power and energy densities. Sulfide solid electrolytes[1–3] are promising for such applications, with Li-argyrodites being particularly noteworthy due to their high ionic conductivities.[4–6] The tunability of the ionic conductivities is achieved by modifying the occupancies of S/X (X = Cl, Br) over the Wyckoff 4d/4a sites.[2,7–9] Based on this design rule, various novel
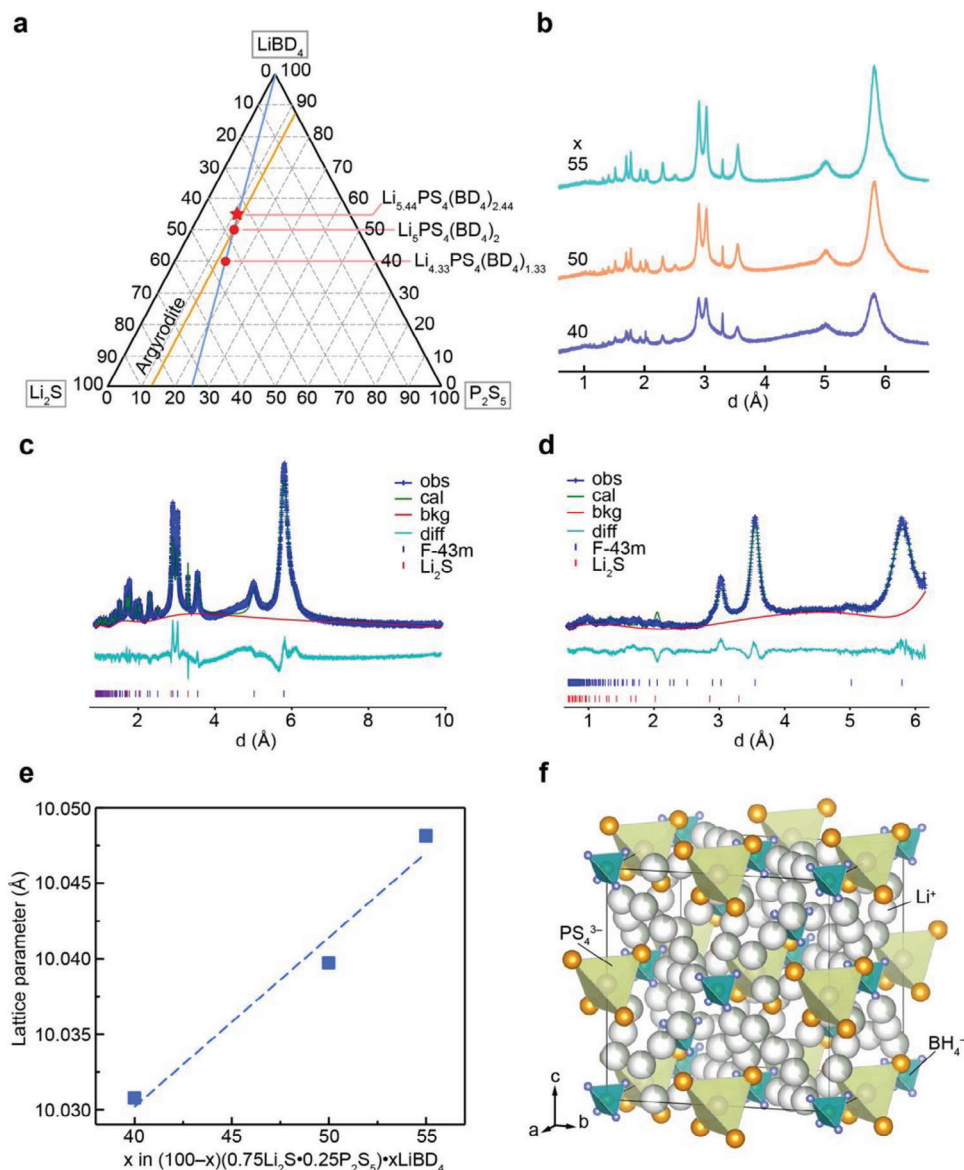
P. Wang, H. Liu, S. Patel, Y. Chen, B. Ogbolu, Y.-Y. Hu
Department of Chemistry and Biochemistry
Florida State University
Tallahassee, FL 32306, USA
E-mail: yhu@fsu.edu
J. E. Roberts, B. E. Francisco
Solid Power, Inc.
Louisville, CO 80027, USA
E-mail: brian.francisco@solidpowerbattery.com
Y.-Y. Hu
Center of Interdisciplinary Magnetic Resonance
National High Magnetic Field Laboratory
Tallahassee, FL 32310, USA

argyrodite compounds with ionic conductivities greater than 10 mS cm^{-1} have been developed, such as Li$_{6-y}$PS$_{5-y}$X$_{1+y}$ (X = Cl, Br),[7,10] Li$_{6+x}$P$_{1-x}$M$_x$S$_5$I,[11–14] and Li$_{6+x}$Sb$_{1-x}$M$_x$S$_5$I[15] (M = Si/Ge). Experimental and theoretical investigations have linked PS$_4^{3-}$ polyhedral rotations with Li$^+$ transport[10,16] and the local arrangements of halides significantly affect PS$_4^{3-}$ rotational rate.[10] With additional degrees of freedom, polyanions, such as BF$_4^-$, BH$_4^-$, and AlH$_4^-$,[17] are promising candidates for engineering the anion frameworks of fast ion conductors. Incorporating polyanions can enhance cation conduction via an enlarged channel size[17] and/or cation-anion dynamical coupling called "paddlewheel"[18–20] effects. However, the co-existence of polyanions and their roles in promoting ion transport remain underexplored. In this paper, we investigate how another polyanion affects the dynamics of PS$_4^{3-}$ and, ultimately, Li$^+$ conduction in argyrodites. We focus on BH$_4^-$ polyanions, characterized by an ionic radius of 2.03 Å. This closely aligns with the ionic radii of I$^-$, Br$^-$, and Cl$^-$, measuring 2.19, 1.96, and 1.81 Å, respectively. This similarity facilitates the fine-tuning of local anion structures without compromising the long-range structure of Li argyrodites.[21,22] In addition, the precursor LiBH$_4$ itself has been considered as a good ion conductor at high temperatures,[23,24] and research efforts have demonstrated the effectiveness of using BH$_4^-$ for improved conductivity.[25–31] More importantly, LiBH$_4$ has a wide voltage stability window,[32,33] which offers a great opportunity to improve the electrochemical stability of sulfide solid electrolytes.[33,34]

BH$_4$-based argyrodite has a complex anion framework composed of BH$_4^-$ and PS$_4^{3-}$.[21] Computational studies have examined cation-polyanion dynamical correlations.[22,35,36] However, these computational findings lack validation through experimental evidence. Additionally, the intricate interplays between BH$_4^-$ and PS$_4^{3-}$ polyanions and their impact on Li$^+$ transport remain largely underexplored. In this work, we synthesized BH$_4$-based Li argyrodites and achieved a high conductivity of 11 S cm^{-1} in Li$_{5.07}$PS$_{4.07}$(BH$_4$)$_{1.93}$. Li$_{5.07}$PS$_{4.07}$(BH$_4$)$_{1.93}$ and derivatives are used as a representative system to understand the dynamical correlations of dual anion systems. To acquire a panoramic picture of the structures and dynamics, multi-nuclear solid-state NMR, relaxometry, high-resolution neutron and X-ray diffraction, and

Figure 1. Long-range structural order of BD_4-based argyrodites, determined with high-resolution X-ray and neutron diffractions. a) BD_4-substituted argyrodite phase diagram. b) High-resolution X-ray Bragg diffraction of BD_4-substituted argyrodites with nominal compositions of (100-x) $(0.75Li_2S \cdot 0.25P_2S_5) \cdot xLiBD_4$, where $x = 40$, 50, and 55. c) Rietveld refinement on the X-ray Bragg diffraction of the nominal $Li_5PS_4(BD_4)_2$. d) Rietveld refinement on the neutron Bragg diffraction of the nominal $Li_5PS_4(BD_4)_2$. e) Lattice parameter as a function of x in (100-x) $(0.75Li_2S \cdot 0.25P_2S_5) \cdot xLiBD_4$. f) The crystal structure of the nominal $Li_5PS_4(BD_4)_2$, obtained from refining the X-ray and neutron Bragg diffractions.

computational methods are employed. The ^2H NMR and NMR relaxometry results unveil that rapid BH_4^- rotations mobilize the anion framework, leading to faster PS_4^{3-} rotations that enhance Li^+ ion transport. Therefore, unlike the commonly observed static disorder in halide-argyrodites, dynamical disorder drives superionic conductivity in BH_4-based argyrodites.

2. Results and Discussion

Three deuterated model compounds with the nominal compositions of $Li_{4.33}PS_4(BD_4)_{1.33}$, $Li_5PS_4(BD_4)_2$, and $Li_{5.44}PS_4(BD_4)_{2.44}$ are synthesized (D stands for deuterium), corresponding to $x = 40$, 50, and 55 in the generalized formula of (100-x) $(0.75Li_2S \cdot 0.25P_2S_5) \cdot xLiBD_4$ (**Figure 1a**). Among them, $Li_5PS_4(BD_4)_2$ has the exact composition as argyrodite $Li_{6-y}PS_{5-y}X_{1+y}$, where X typically represents a halide anion, such as Cl^-, Br^-, I^-, or a combination thereof. To examine the long-range structural order, neutron and high-resolution X-ray diffraction characterizations are performed. Figure 1b shows the high-resolution X-ray diffraction of $Li_{4.33}PS_4(BD_4)_{1.33}$, $Li_5PS_4(BD_4)_2$, and $Li_{5.44}PS_4(BD_4)_{2.44}$. The Rietveld refinement of the X-ray (Figure 1c) and neutron (Figure 1d) diffractions reveals that the structures adopt the $F\bar{4}3m$ space group with PS_4^{3-} and BH_4^- interspersed, as presented in Figure 1f. The main phase

ADVANCED
SCIENCE NEWS

www.advancedsciencenews.com

ADVANCED
ENERGY
MATERIALS

www.advenergymat.de

Table 1. Compositions, main phase fractions, and boron occupancies at 4a/4d sites of the BD$_4$-substituted argyrodites obtained by refining the X-ray and neutron diffractions.

BD$_4$ content x in (100-x) (0.75Li$_2$S·0.25P$_2$S$_5$)·xLiBD$_4$	Nominal composition	Experimentally determined composition	Main phase fraction [%]	BD$_4$ occupancy at 4a/4d
40	Li$_{4.33}$PS$_4$(BD$_4$)$_{1.33}$	Li$_{5.01}$PS$_{4.19}$(BD$_4$)$_{1.63}$	95.0	0.91/0.72
50	Li$_{5.00}$PS$_4$(BD$_4$)$_{2.00}$	Li$_{5.19}$PS$_{4.19}$(BD$_4$)$_{1.81}$	96.6	1/0.81
55	Li$_{5.44}$PS$_4$(BD$_4$)$_{2.44}$	Li$_{5.07}$PS$_{4.07}$(BD$_4$)$_{1.93}$	97.5	1/0.93

in the nominal Li$_{5.00}$PS$_4$(BD$_4$)$_{2.00}$ has an actual composition of Li$_{5.19}$PS$_{4.19}$(BD$_4$)$_{1.81}$, based on the refinement. Increasing BD$_4$ content results in an expanded unit cell (Figure 1e). Furthermore, a higher BD$_4$ content is associated with increased peak intensities, as shown in Figure 1b, indicating enhanced crystallinity. As shown in **Table 1**, the highest argyrodite phase purity of 97.5% is obtained in Li$_{5.07}$PS$_{4.07}$(BD$_4$)$_{1.93}$ (x = 55), which implies that extra BD$_4$ (x > 50) is beneficial to compensating for thermal loss of BD$_4^-$ and for obtaining a high phase purity. It is worth noting that Li$_{5.07}$PS$_{4.07}$(BD$_4$)$_{1.93}$ (x = 55) has the highest 4d site occupancy of 0.93 among the three compositions. The SEM images of Li$_{5.01}$PS$_{4.19}$(BD$_4$)$_{1.63}$ (x = 40), Li$_{5.19}$PS$_{4.19}$(BD$_4$)$_{1.81}$ (x = 50), and Li$_{5.07}$PS$_{4.07}$(BD$_4$)$_{1.93}$ (x = 55) are acquired and presented in Figure S4 (Supporting Information). With an increasing content of BD$_4$, the particles become smaller and packed denser (Figure S4, Supporting Information).

To evaluate the Li$^+$ conduction in the BD$_4$-substituted argyrodites, the conductivities are calculated based on the AC electrochemical impedance measurements. The results reveal that Li$_{5.07}$PS$_{4.07}$(BD$_4$)$_{1.93}$ has the highest ionic conductivity of 8.36 mS cm^{-1} in the series, which is higher than that of Li$_6$PS$_5$Cl[9] and Li$_6$PS$_5$Br[8] (**Table 2**). Compared to Li$_6$PS$_5$Cl/Br, the merit of Li$_{5.07}$PS$_{4.07}$(BD$_4$)$_{1.93}$ also lies in its low mass density, which is 1.534 g cm^{-3}, compared with 1.852 g cm^{-3} for Li$_6$PS$_5$Cl and 2.016 g cm^{-3} for Li$_6$PS$_5$Br. Therefore, BH$_4$-substituted argyrodites are promising for achieving a higher gravimetric energy density.

As aforementioned, the most conductive sample Li$_{5.07}$PS$_{4.07}$(BD$_4$)$_{1.93}$ has the highest 4a/4d site occupancy by BD$_4$. Thus, the origin of its high conductivity can be different from halide argyrodites,[7–9,12] i.e., the fast conduction is correlated to the significant S^{2-}/X$^-$ vacancies and exchange over the 4a/4d sites. To understand the effects of 4a/4d site occupancy on ion conduction, the Li tracer diffusivity is calculated for the structures with and without BH$_4^-$ vacancies via ab initio

Table 2. The ionic conductivities and densities of (100-x) (0.75Li$_2$S·0.25P$_2$S$_5$)·xLiBD$_4$ (x = 40, 50, and 55), Li$_6$PS$_5$Cl, and Li$_6$PS$_5$Br. The chemical compositions and densities are obtained by refining the high-resolution X-ray diffractions.

| Composition	Density [g cm^{-3}]	Ionic conductivity [mS cm^{-1}]
Li$_{5.01}$PS$_{4.19}$(BD$_4$)$_{1.63}$	1.512	2.29 (this work)
Li$_{5.19}$PS$_{4.19}$(BD$_4$)$_{1.81}$	1.549	4.86 (this work)
Li$_{5.07}$PS$_{4.07}$(BD$_4$)$_{1.93}$	1.534	8.36 (this work)
Li$_6$PS$_5$Cl	1.852	7.31[9]
Li$_6$PS$_5$Br	2.016	5.48[8]

molecular dynamics (AIMD) simulations. The result is evident that BH$_4^-$ vacancies lead to slower ion conduction and a higher activation energy of 0.18 eV compared with 0.14 eV of the pristine structure (**Figure 2a**). Therefore, the fully occupied 4a/4d sites are consistent with the higher ionic conductivity of Li$_{5.07}$PS$_{4.07}$(BD$_4$)$_{1.93}$ and Li$_{5.19}$PS$_{4.19}$(BD$_4$)$_{1.81}$.

As mentioned previously, the 4a-site occupancy is higher than the 4d-site in all compounds, indicating a potential BH$_4^-$ site preference. Here, the energy above hull (E_{hull}) of the structures with BH$_4^-$ vacancies on different sites is calculated for a quantitative measurement of structural stability. The results documented in Table S1 (Supporting Information) show that the E_{hull} for the structures with vacancies at either the 4a or 4d sites is low, <50 meV, with a slightly higher E_{hull} for vacancies at 4a sites.[37–39] This suggests BH$_4^-$-deficient structures can readily form and exhibit relatively low conductivity.

As the local structural order can greatly affect the ion conduction in solid electrolytes,[40] neutron pair distribution function (nPDF), [G(r)], is employed to examine the short-range structures in BD$_4$-substitued argyrodites (**Figure 3**). The B-D correlation at ≈1.2 Å shows an increased intensity in Li$_{5.19}$PS$_{4.19}$(BD$_4$)$_{1.81}$ and Li$_{5.07}$PS$_{4.07}$(BD$_4$)$_{1.93}$ (x = 50 and 55), consistent with the higher BD$_4$ content. From x = 40 to 55 in (100-x) (0.75Li$_2$S·0.25P$_2$S$_5$)·xLiBD$_4$, the P–B correlation peak displays both an increased intensity and a more diffused feature, suggesting an increased BD$_4^-$ content and local disorder. The negative peak at 1.6–1.8 Å corresponds to the Li-D correlation. the broadening of this peak for x = 50 and 55 indicates a broad distribution of Li-BD$_4$ distances.

The nPDF results (Figure 3) reveal Li arrangement is sensitive to the change in the anion framework. Li NMR serves as an excellent probe to examine Li-anion interactions. Specifically, ^{6}Li NMR is employed due to its higher spectral resolution than ^{7}Li NMR. In **Figure 4a**, the ^{6}Li resonances of BD$_4$-substituted argyrodites are between those of glassy-Li$_3$PS$_4$ and LiBH$_4$. This positioning suggests that Li$^+$ ions effectively traverse among the PS$_4^{3-}$ and BD$_4^-$ units. With an increased concentration of BD$_4$, the ^{6}Li resonance shifts towards a higher field closer to the resonance of LiBH$_4$, signifying an overall greater residential time of Li$^+$ near BD$_4^-$ anions (Figure 4a). Two ^{6}Li resonances are resolved via detailed spectral analysis in all the BD$_4$-substituted-argyrodites (Figure 4a) and assigned as Li (I) and Li (II). The Li (II) resonance is located more centered between Li$_3$PS$_4$ and LiBD$_4$ peaks compared with Li (I), indicating that Li (II) has a more balanced interaction with PS$_4^{3-}$ and BD$_4^-$ anions. Presented in Figure 4b are the fractions of Li (I) and Li (II), where an increased fraction of Li (II) is seen with a higher

BD$_4$ concentration. To validate the ^{6}Li NMR spectral assignments, the ^{6}Li density functional theory (DFT) NMR calculations
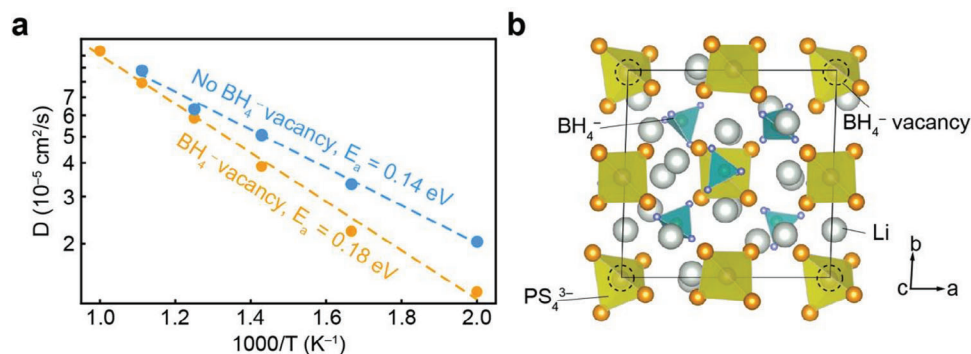
Figure 2. Effects of BH_4 vacancies on ion conduction. a) Arrhenius plots of the calculated Li^+ tracer diffusion coefficients versus temperature for structures without and with BH_4 vacancies (25%). b) The crystal structure with 25% BH_4 vacancies was used in the calculation.

are performed on $(100-x)$ $(0.75Li_2S \cdot 0.25P_2S_5) \cdot x LiBD_4$ with $x = 46.7$, 48.4, and 50 (Figure S5, Supporting Information). The results show one resonance at ≈0.3 ppm corresponding to Li (II) and the other one at ∼1.3 ppm corresponding to Li (I). With an increased BD_4 concentration, the fraction of Li (I) decreases, together with a shift towards a higher field (Figure S5, Supporting Information), which agrees with the experiment results (Figure 4a). The local coordination environments around Li (I) and Li (II) in the structure used for the DFT NMR calculations are presented in Figure 4b. Both Li (I) and Li (II) are surrounded by BD_4^- and PS_4^{3-} anions. Li (I) has three neighboring Li atoms, while Li (II) has two other Li ions, consistent with our previous observations in halide-based argyrodite materials that Li^+ with fewer neighboring Li^+ has a smaller chemical shift.[7–10] In addition, these Li^+ ions often exhibit higher mobility and a larger contribution to ionic conductivity in halide-based argyrodites.[8,9] The DFT calculation results reveal that the ^6Li shift is correlated with the number of neighboring BH_4^- anions (Table S3 and Figure S11, Supporting Information). More BH_4^- anions around lead to a smaller average ^6Li shift. Thus, the Li (I) resonance from the NMR experiments corresponds to the Li surrounded by fewer BH_4^- anions, compared with Li (II).
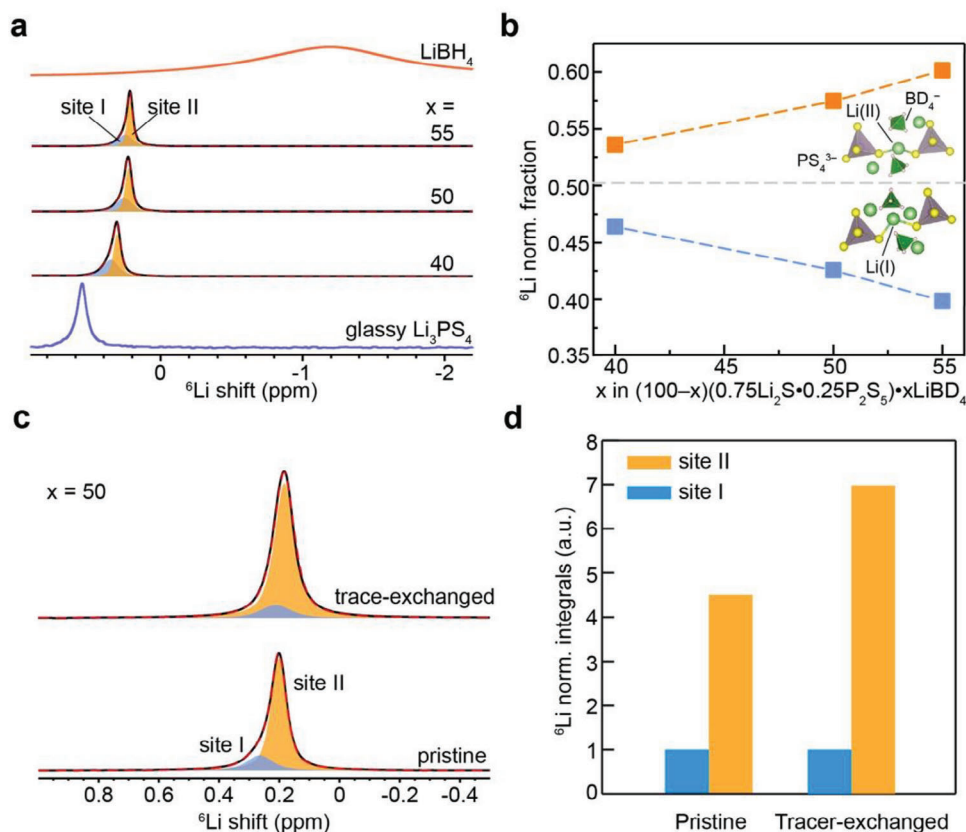
To determine the role of Li (I) and Li (II) in ion conduction, the electrochemically driven $^6Li \rightarrow {^7Li}$ tracer exchange NMR[8,41] is employed (Figure 4c), where the solid electrolyte pellet is sandwiched by two ^6Li-rich electrodes and cycled with a biased potential. ^7Li on the transport pathways will be replaced by ^6Li from the electrodes after electrochemical cycling. Thus, the Li sites that participate in ion conduction can be identified via quantitative analysis of $^{6,7}Li$ NMR before and after tracer exchange, i.e., Li sites that participate in ion transport will show increased ^6Li isotope content.[8] The quantitative analyses (Figure 4d) of ^6Li NMR on $Li_{5.19}PS_{4.19}(BD_4)_{1.81}$ before and after tracer exchange reveals an evident increase in the ^6Li abundance of Li (II) in the tracer-exchanged sample, while that of Li (I) remains the same. Thus, Li (II) is more involved in Li^+ conduction.

The BH_4/BD_4-substituted argyrodites have structural attributes and conduction properties different from their halide counterparts. BH_4/BD_4 incorporation alters the anion frameworks. Here, ^{31}P and ^{11}B NMR are employed to gain insights into the short-range arrangements of the two building blocks: PS_4^{3-} and BD_4^-. **Figure 5a** shows the ^{31}P NMR comparison between the $Li_{5.01}PS_{4.19}(BD_4)_{1.63}$ $(x = 40)$ sample and glassy Li_3PS_4. The ^{31}P resonance at ≈84 ppm is assigned to PS_4^{3-} in a non-interrupted PS_4^{3-} network.[42] The minor resonance at ≈108 ppm is from $P_2S_6^{4-}$, which does not change across all the BD_4-substituted argyrodites. The new resonance at ≈90 ppm originates from PS_4^{3-} with BD_4^- interspersed, denoted as $PS_4^{3-} \cdots BD_4^-$, which grows with increasing the BD_4 content (Figure 5a). The ^{31}P NMR of the BH_4 analogs $(x = 40, 50, \text{and } 55)$ is acquired (Figure S8,
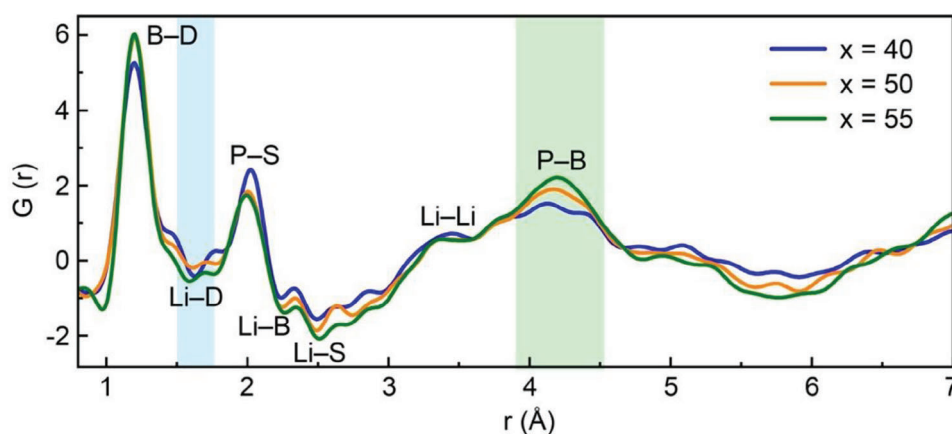
Figure 3. Short-range structural order of $(100-x)$ $(0.75Li_2S \cdot 0.25P_2S_5) \cdot x LiBD_4$ $(x = 40, 50, \text{and } 55)$ revealed by neutron pair distribution function analysis.

**ADVANCED
SCIENCE NEWS**

www.advancedsciencenews.com

**ADVANCED
ENERGY
MATERIALS**

www.advenergymat.de

Figure 4. Li local structures in BD_4-based argyrodites. a) ^6Li MAS NMR spectra of $(100\text{-}x)$ $(0.75Li_2S\cdot0.25P_2S_5)\cdot xLiBD_4$ ($x = 40$, 50, and 55). b) Quantified fractions of Li (I) and Li (II) based on the areal integrals of their ^6Li NMR resonances shown in (a). c) ^6Li NMR spectra of the pristine and the tracer-exchanged sample when $x = 50$, i.e., $Li_{5.19}PS_{4.19}(BD_4)_{1.81}$. d) Relative ^6Li-enrichment of Li(I) and Li (II) sites after $^6Li \rightarrow ^7Li$ tracer exchange. The ^6Li NMR areal integrals are normalized based on the areal integral of Li (I) in the pristine sample.
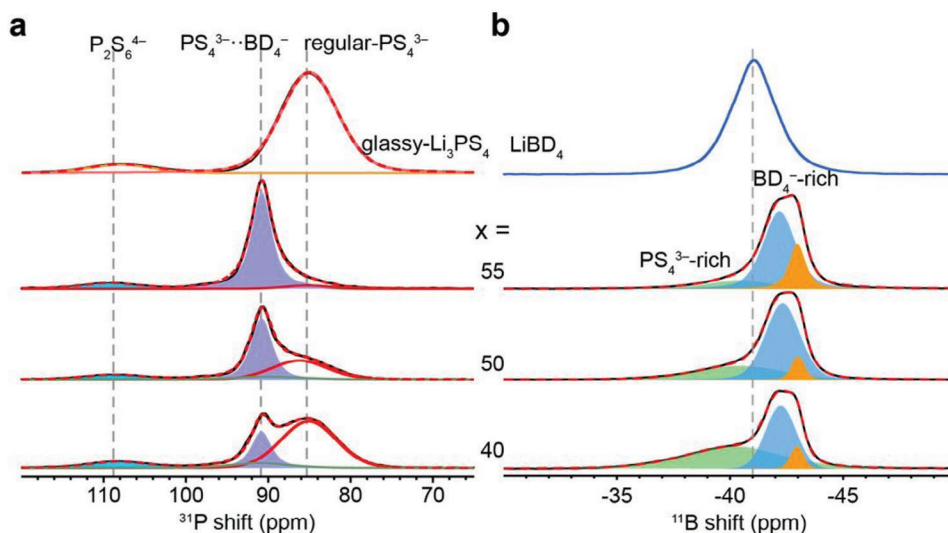
Figure 5. Anion sublattice local arrangements of BD_4-based argyrodites probed with MAS NMR, suggesting BH_4^- interspersed within the PS_4^{3-} matrix and increased PS_4^{3-} rotational rate. a) ^{31}P NMR and b) ^{11}B NMR spectra of $(100\text{-}x)$ $(0.75Li_2S\cdot0.25P_2S_5)\cdot xLiBD_4$ ($x = 40$, 50, and 55).

Supporting Information), showing the same trend of the 90-ppm peak fraction with increasing the BH_4 content. The fraction of PS_4^{3-} with BD_4^- interspersed positively correlates to the conductivity, indicating a critical role of BD_4^- in promoting fast Li^+ conduction.

^{11}B NMR is utilized to investigate the BD_4 sub-lattice. Figure 5b shows that the BD_4-substituted argyrodites have distinct [11]B local environments from $LiBD_4$. Three [11]B resonances in the BD_4-substituted argyrodites are observed. It is noted that the trend of the −40 ppm peak (Figure 5b) echoes with that of regular PS_4^{3-} (Figure 5a), suggesting that this resonance arises from the BD_4^- in a PS_4^{3-}-rich environment. Similarly, the −42-ppm peak intensity increases as the fraction of $PS_4^{3-}\cdot\cdot BD_4^-$ grows, indicating that it is the BD_4^- in a relatively BD_4^--rich argyrodite framework. The ^{11}B NMR of the BH_4 analogs (x = 40, 50, and 55) is presented in Figure S7 (Supporting Information), where an increasing fraction of the BH_4^--rich environment is also seen. The −43-ppm resonance (orange, in Figure 5b) is also a BD_4-rich local environment, likely arising from the local aggregation of BD_4 in the anion sublattice. In contrast, the BH_4 distribution in the structure is relatively more homogeneous; thus, the intensity of the −43 ppm resonance is lower in the BH_4 analogs (Figure S7, Supporting Information).

To confirm the assignments of resonances observed in the ^{31}P and ^{11}B NMR (Figure 5), we have carried out DFT NMR calculations. The calculated ^{31}P spectra of $Li_5PS_4(BD_4)_2$ and $Li_{4.75}PS_4(BD_4)_{1.75}$ with BD_4 vacancies at the 4a/4d sites are shown in Figure S6a (Supporting Information). The highlighted area (^{31}P shift < 90 ppm) reveals that $Li_5PS_4(BD_4)_2$ without vacancies at the 4a/4d sites (high BD_4 content) has a more homogenized signal, while the two compounds with vacancies both show two resonances in this region. This is in accordance with the experiment (Figure 5a). Moreover, the calculated ^{11}B NMR spectra of the structures with different BD_4 contents (x = 46.7, 48.4, and 50) are displayed in Figure S6b (Supporting Information). The x = 46.7 sample has two distinctive resonances. However, the x = 48.4 and 50 show merging [11]B signals in the highlighted area, consistent with experimental spectra presented in Figure 5b.

To understand the ion conduction and its origin in the BH_4-substituted argyrodites, electrochemical impedance spectroscopy and NMR relaxometry are employed. **Figure 6a** shows the conductivity of the BH_4-(x = 40, 50, 55, and 60) and BD_4-(x = 40, 50, and 55) substituted compounds. Within the range of x = [40, 55], the BH_4- and BD_4-substituted argyrodites exhibit higher conductivities with increased BH_4/BD_4 content. The highest conductivity of 11 mS cm^{-1} is achieved in $Li_{5.07}PS_{4.07}(BH_4)_{1.93}$ (x = 55). With the same BH_4/BD_4 content, the BH_4-substituted argyrodites always have a higher conductivity than the BD_4 counterpart. A BH_4 concentration of $x > 60$ results in a decreased conductivity. The activation energy of the BH_4-substituted argyrodites is shown in Figure 6a, which is within the range of 0.32 to 0.35 eV.

To understand the dynamic origin of the observed ionic conductivities in the BH_4- and BD_4-substituted argyrodites, variable-temperature [7]Li spin-lattice relaxation time is measured to investigate the Li^+ dynamics (**Figure 7a**, bottom). In general, an NMR relaxometry plot (T$_1$ vs 1000/T) consists of two rate regions dependent on $\omega_0\tau_c$[10] (ω_0, the Larmor frequency; τ_c, the correlation time): 1) a fast-motion region ($\omega_0\tau_c$ << 1) and 2) a slow-motion region ($\omega_0\tau_c$ >> 1). When $\omega_0\tau_c \approx 1$, the T$_1$ is
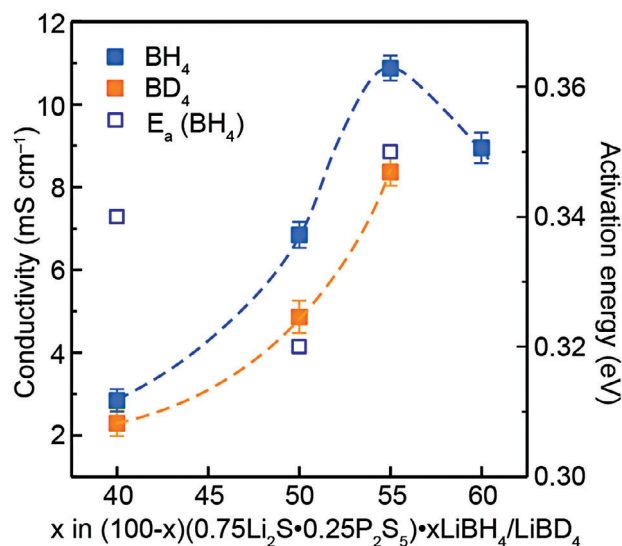
Figure 6. Ionic conductivity of the nominal (100-x) (0.75Li$_2$S·0.25P$_2$S$_5$)·LiBH$_4$/LiBD$_4$ (x = 40, 50, and 55) at 22 °C.

the smallest and signals a transition between the slow-motion region and the fast-motion region. The temperatures to reach $\omega_0\tau_c \approx 1$, denoted in Figure 7a, are 94, 45, and 34 °C for (100-x) (0.75Li$_2$S·0.25P$_2$S$_5$)·LiBH$_4$ with x = 40, 50, and 55, respectively. A lower temperature is required to enable fast Li^+ conduction ($\omega_0\tau_c$ << 1) in the compounds with a higher BH_4 content, indicating faster Li^+ motion in them, which echoes with the higher conductivity found in $Li_{5.07}PS_{4.07}(BH_4)_{1.93}$ (x = 55) (Figure 6a). The [7]Li T$_1$ for the BD_4 and the BH_4 analogs with x = 50 are compared in Figure S1a (Supporting Information). The temperature for reaching $\omega_0\tau_c \approx 1$ in the BH_4 analog (45 °C) is lower than that of the BD_4 analog (55 °C), indicating faster Li^+ motion in the BH_4-substituted argyrodites. The room-temperature [7]Li T$_1$ of the BD_4 and the BH_4 analog with x = 40, 50, and 55 are shown in Figure S1b (Supporting Information). The shorter T$_1$ for x = 40 and 50 (slow motion region), and the longer T$_1$ for x = 55 (fast motion region) in the BH_4 analogs are observed (Figure S1b, Supporting Information), suggesting that the BH_4 analogs always have faster Li^+ motion than the BD_4 analogs.

To determine the effects of polyanion-PS_4^{3-} and BH_4^--dynamics on Li^+ conduction in the BH_4-substituted argyrodites, ^{31}P NMR relaxometry and static ^{2}H NMR are employed. As two different PS_4^{3-} units are observed in the ^{31}P NMR spectra (Figure 5a), their relaxometry behaviors are presented separately. Figure 7a reveals that all three samples have fast PS_4^{3-} rotation for $PS_4^{3-}\cdot\cdot BH_4^-$, because only the fast-motion region ($\omega_0\tau_c$ << 1) is shown within the range of [34 °C, 104 °C] (Figure 5a, top panel). For the regular PS_4^{3-}, high temperatures are required for the transition to the fast-motion region, i.e., 54 °C and 64 °C for x = 40 and x = 50 compositions, respectively, suggesting that the motions of the regular PS_4^{3-} tetrahedra (middle panel, Figure 7a) is slower than $PS_4^{3-}\cdot\cdot BH_4^-$. To investigate the potential correlation between Li^+ and PS_4^{3-}, the [7]Li T$_1$ (bottom panel, Figure 7a) is compared with the [31]P T$_1$. It is worth noting that the intermediate motion region ($\omega_0\tau_c \approx 1$) for Li^+ and PS_4^{3-} ($PS_4^{3-}\cdot\cdot BH_4^-$) occur at a

ADVANCED
SCIENCE NEWS
www.advancedsciencenews.com

ADVANCED
ENERGY
MATERIALS
www.advenergymat.de
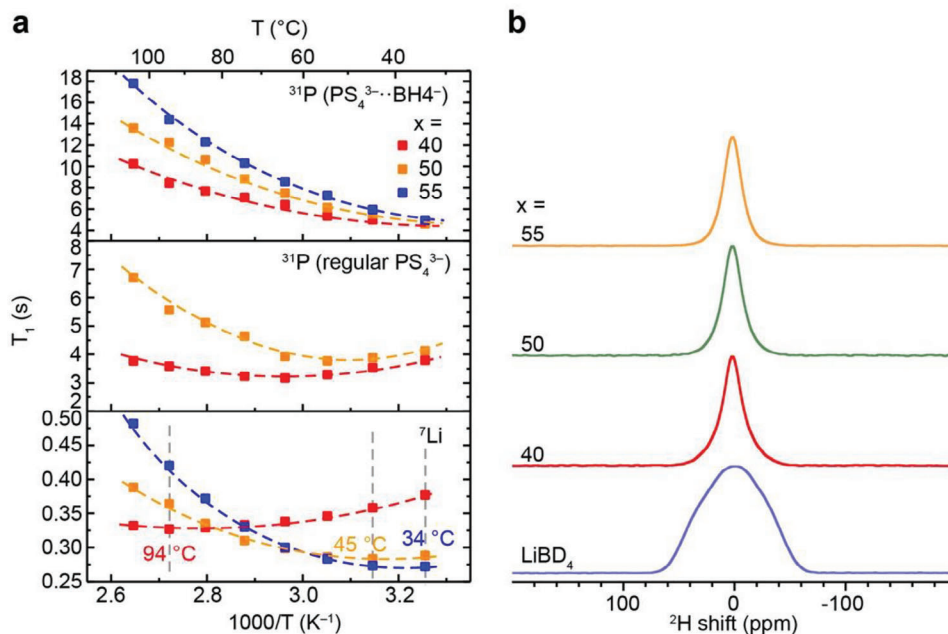
Figure 7. PS_4^{3-} and BH_4^- anion dynamics in $(100-x)(0.75Li_2S\cdot0.25P_2S_5)\cdot xLiBH_4$ ($x = 40$, 50, and 55) and their impact on Li^+ ion dynamics. a) ^{31}P T_1 of $PS_4^{3-}\cdots BH_4^-$ and regular PS_4^{3-} compared with ^7Li T_1 ($x = 40$, 50, 55), suggesting increased Li^+ and PS_4^{3-} motions with x. b) Static ^2H NMR spectra of $(100-x)(0.75Li_2S\cdot0.25P_2S_5)\cdot xLiBD_4$ ($x = 40$, 50, 55); the narrowed linewidth is induced by enhanced BD_4 rotational motion.

similar temperature for $Li_{5.07}PS_{4.07}(BD_4)_{1.93}$ ($x = 55$), indicating a correlated motion between the Li^+ and PS_4^{3-}. However, this is not observed for the $x = 40$ and 50 compositions, which may explain their lower ionic conductivity. The ^{31}P T_1 for the BD_4 and the BH_4 analogs with $x = 50$ are compared in Figure S3a (Supporting Information). The PS_4^{3-} motion in the BH_4 analog is faster than the BD_4 counterpart, revealed by the longer ^{31}P T_1 for $PS_4^{3-}\cdots BH_4^-$ in BH_4-substituted argyrodite (Figure S3a, Supporting Information). Moreover, the longer ^{31}P T_1 of all the BH_4-substituted argyrodites suggests faster PS_4^{3-} motion (Figure S3b, Supporting Information), compared with the BD_4 analogs. The static ^2H NMR spectra of BD_4-substituted argyrodites ($x = 40$, 50, and 55) are compared to $LiBD_4$ (Figure 7b). The narrower line widths of the ^2H NMR resonances of the three BD_4-substituted argyrodites suggest that the BD_4^- motion in the argyrodite structures is faster than that of $LiBD_4$. The ^2H signal of $Li_{5.07}PS_{4.07}(BD_4)_{1.93}$ ($x = 55$) exhibits the narrowest linewidth (Figure S9, Supporting Information), indicating the fastest BD_4^- motion. The time scale of BD_4 can be estimated using Equation 1,[43] where T_2 is the spin–spin relaxation time constant, which can be calculated using $T_2 = \frac{1}{\pi\Delta\nu}$ ($\Delta\nu$: full width at half maximum), C_Q is the quadrupolar coupling constant, $\omega_0 = \gamma B_0$ is the Larmor frequency, and τ_c is the correlation time.

$$\left(\frac{1}{T_2}\right) = \frac{3\pi^2}{2} C_Q^2 \left[\frac{3}{2}\tau_c + \frac{3}{2}\cdot\frac{\tau_c}{1+\omega_0^2\tau_c^2} + \frac{\tau_c}{1+4\omega_0^2\tau_c^2}\right] \quad (1)$$
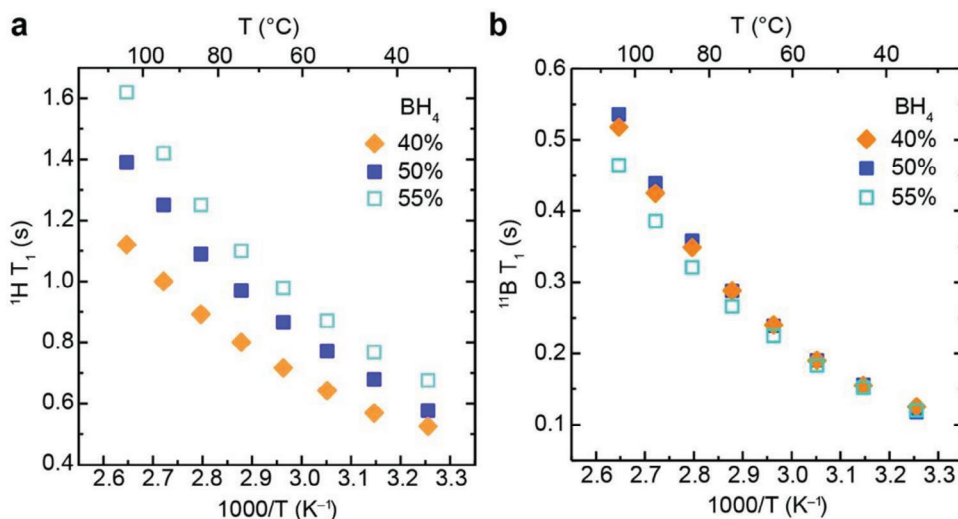
With $\omega_0\tau_c \ll 1$, Equation 1 can be simplified to

$$\left(\frac{1}{T_2}\right) = 6\pi^2 C_Q^2 \tau_c \quad (2)$$

Thus, the estimated time constant for BD_4^- rotation in $Li_{5.07}PS_{4.07}(BD_4)_{1.93}$ ($x = 55$) is 1.30×10^{-9} s ($T_2 = 2.17 \times 10^{-4}$ s, $C_Q = 245$ kHz, Figure S10 and Table S2, Supporting Information). The variable-temperature ^1H and ^{11}B T_1 (**Figure 8**) relaxation times are measured to further investigate the dynamics of BH_4^- in $(100-x)(0.75Li_2S\cdot0.25P_2S_5)\cdot xLiBH_4$ ($x = 40$, 50, and 55). As shown in Figure 8a, the ^1H T_1 of the three compounds falls in the fast motion region ($\omega_0\tau_c \ll 1$), where a longer T_1 indicates a faster motion. Therefore, $Li_{5.07}PS_{4.07}(BH_4)_{1.93}$ ($x = 55$) has the fastest BH_4 motion, which is consistent with the ^2H NMR line width analysis (Figure 7b). Since the ^1H–^1H dipolar coupling is the dominant interaction that drives ^1H T_1 relaxation here, the time of BH_4^- motion (τ_c) can be estimated using Equation 3,[10] where γ is the magnetogyric ratio, $\hbar$ is the reduced Plank's constant, r_0 is the interatomic distance, and μ_0 is the vacuum permeability.

$$\left(\frac{1}{T_1}\right) = \frac{3}{2}\frac{\gamma^4\hbar^2\mu_0^2}{r_0^6}\tau_c \quad (3)$$

Thus, the estimated τ_c is 1.13×10^{-9} s at 34 °C (H–H distance $r_0 = 2.01$ Å, $T_1 = 0.676$ s), similar to the motional time constant calculated based on ^2H NMR. The ^{11}B T_1 relaxation times of the three samples are similar (Figure 8b); this is because the BH_4^- motional rate, estimated 885.0 MHz at 34 °C, is much larger than the ^{11}B Larmor frequency, 96.3 MHz, making the ^{11}B T_1 less sensitive to the variations in BH_4^- rotational rates compared with ^1H T_1. The ^1H and ^{11}B T_1 values are acquired for the analogs with 50% BH_4 and BD_4 (Figure S2, Supporting Information). Both samples show fast BH_4^- motion. A longer ^1H T_1 is observed in the BD_4 analog (Figure S2a, Supporting Information), because of its smaller ^1H-^2H hetero-nuclear dipolar coupling compared

**ADVANCED
SCIENCE NEWS**

www.advancedsciencenews.com

**ADVANCED
ENERGY
MATERIALS**

www.advenergymat.de

Figure 8. Variable-temperature a) ^{1}H and b) ^{11}B T_1 of $(100\text{-}x)$ $(0.75Li_2S\cdot0.25P_2S_5)\cdot xLiBH_4$ ($x = 40$, 50, and 55).

with the ^{1}H–^{1}H coupling in the BH_4 analog (Equation 3, $\gamma_{1H} = 42.6$ MHz T^{-1}, $\gamma_{2H} = 6.5$ MHz T^{-1}). The ^{11}B T_1 for the BH_4/BD_4 analogs is almost the same (Figure S2b, Supporting Information), consistent with the observation shown in Figure 8b.

The BH_4^- rotational rates in the BH_4-substituted argyrodites, approximately on the order of ~GHz, are nearly 10 times the PS_4^{3-} rotational rates and Li motion, which are on the order of 100 MHz. It suggests that only PS_4^{3-} rotations directly correlate with Li diffusion. However, it is evident that faster BH_4^- rotation is positively correlated with faster PS_4^{3-} rotations. Therefore, the BH_4^- in the argyrodite structures acts as a small gear with rapid rotation, driving the rotation of the larger PS_4^{3-}, and in turn, promoting Li diffusion.

The performance of $(100\text{-}x)$ $(0.75Li_2S\cdot0.25P_2S_5)\cdot xLiBH_4$ ($x = 55$) as a component of the composite cathode (catholyte) to promote ion transport is evaluated in NMC622 | Li ASSBs (**Figure 9**). As shown in Figure 9a, the cell with $(100\text{-}x)$ $(0.75Li_2S\cdot0.25P_2S_5)\cdot xLiBH_4$ ($x = 55$) has a slightly lower initial specific capacity than Li_6PS_5Cl (187.8 vs 189.7 mAh g^{-1}) but exhibits a slower capacity fade. After 42 cycles, the cells with $(0.75Li_2S\cdot0.25P_2S_5)\cdot xLiBH_4$ ($x = 55$) and Li_6PS_5Cl show a capacity retention of 101.6% and 97.2%, respectively. The

$(0.75Li_2S\cdot0.25P_2S_5)\cdot xLiBH_4$ ($x = 55$) cell has an initial coulombic efficiency (CE) of 93.5%, which is higher than that of the cell using Li_6PS_5Cl (90.9%). At Cycle 42, the CE of the BH_4-argyrodite cell is 99.9%, compared with 99.3% for Li_6PS_5Cl (Figure 9b). Therefore, BH_4-argyrodite outperforms Li_6PS_5Cl in ASSBs. Figure 9c shows that after 42 cycles, the cell resistance of the BH_4-argyrodite cell is increased by 32%, which is lower than 258% for argyrodite. The slower increase in cell resistance and the higher CE indicate that BH_4-argyrodite is more stable against NMC622 than Li_6PS_5Cl, which results in better cell performance.

3. Conclusion

A series of compounds are synthesized using Li_2S, P_2S_5, and $LiBH_4$, yielding a high ionic conductivity of 11 mS cm^{-1} in $Li_{5.07}PS_{4.07}(BH_4)_{1.93}$. The BD_4-analogs are also created to investigate their structures using neutron diffraction. Structurally, these compounds adopt the argyrodite framework in the $F43m$ space group, with interspersed PS_4^{3-} and BH_4^-. In contrast to the extensively studied halide-based argyrodite ion conductors, BH_4-based argyrodites achieve high ionic conductivity and low activation energy when the 4a/4d Wycoff sites are fully occupied
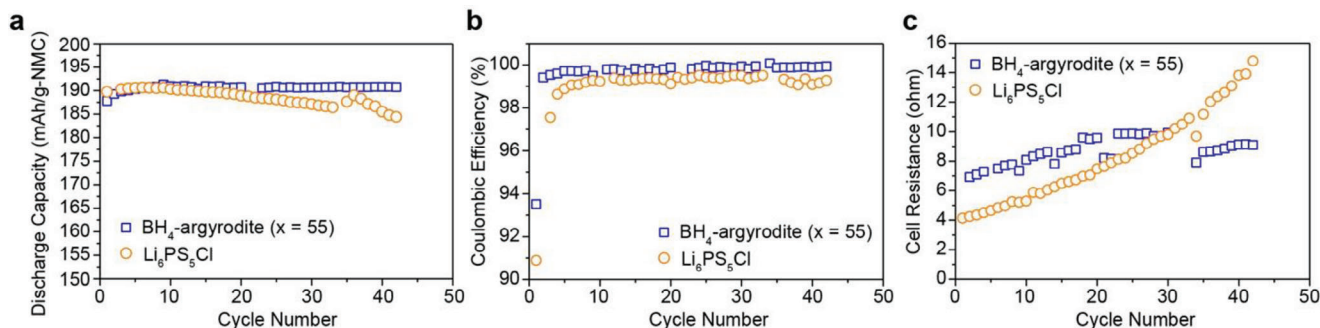
Figure 9. Performance comparison of NMC622 | $Li_{10}P_3S_{12}I$ | Li all-solid-state batteries using $(100\text{-}x)$ $(0.75Li_2S\cdot0.25P_2S_5)\cdot xLiBH_4$ ($x = 55$) and Li_6PS_5Cl in the composite cathode, cycled with a current of 18.0 mA g^{-1}. a) Discharge capacity, b) Coulombic efficiency, and c) cell resistance versus cycle number are presented with blue squares and orange circles for $(100\text{-}x)$ $(0.75Li_2S\cdot0.25P_2S_5)\cdot xLiBH_4$ ($x = 55$)- and Li_6PS_5Cl-containing battery cells, respectively.

by BH_4 with limited static disorder. The maximum dispersion of PS_4^{3-} and BH_4^- within the anion lattice allows Li^+ interactions with both polyanions, as revealed by the weighted ^6Li chemical shift. Li sites with more neighboring BH_4^- and balanced interactions with PS_4^{3-} and BH_4^- dominant ion conduction. Dynamically, BH_4^- exhibits rapid rotation on the GHz scale, while PS_4^{3-} rotates with a much slower rate of ~100 MHz. However, faster BH_4^- rotation correlates with more rapid PS_4^{3-} rotation. PS_4^{3-} rotation occurs on a similar time scale with Li motion and closely correlates with the observed ion conduction. Therefore, BH_4-based argyrodites exhibit a unique dual motor mechanism, yielding superionic transport. Furthermore, the performance of BH_4-based argyrodites used in composite cathodes with NMC622 as the active material is evaluated, and it exhibits improved electrochemical and long-term cycling stability compared with the Cl-based argyrodite Li_6PS_5Cl. This experimental investigation provides valuable insights for theoretical studies of dual-polyanion ion conductors and practical efforts in designing and synthesizing high-performance superionics leveraging the uncovered mechanisms.

4. Experimental Section

Synthesis: $(100\text{-}x)$ $(0.75Li_2S\cdot0.25P_2S_5)\cdot xLiBH_4$ ($x = 40, 50, 55,$ and 60) and $(100\text{-}x)$ $(0.75Li_2S\cdot0.25P_2S_5)\cdot xLiBD_4$ ($x = 40, 50,$ and 55) electrolytes were synthesized via planetary ball milling. Stoichiometric amounts of Li_2S (Sigma Aldrich), P_2S_5 (Acros Organics), and $LiBH_4$ (Sigma Aldrich)/ $LiBD_4$ (Katchem) were loaded into ZrO_2 milling jars with 5 mm ZrO_2 media and anhydrous xylene (Sigma Aldrich) as a processing aid. Milling was carried out using a Retsch PM100 mill for 12 h at 500 rpm. After milling, xylene was removed under a vacuum at 70 °C for 2 h.

Solid-State NMR Measurements: ^6Li, ^{11}B, and ^{31}P NMR magic-angle-spinning (MAS) NMR experiments were performed on a Bruker Avance III-500 spectrometer with a magnetic field of 11.75 T. The Larmor frequencies are 73.58, 160.4, and 202.4 MHz for ^6Li, ^{11}B and ^{31}P, respectively. The powdered electrolyte samples were packed in 2.5 mm rotors and spun at 25 kHz. The ^6Li spectra were collected with a $\pi/2$ pulse of 4.75 µs. The ^6Li shifts were referenced to $LiCl_{(s)}$ at -1.1 ppm. For ^{31}P NMR, a rotor-synchronized spin-echo sequence of 4.2–8.4 µs ($\pi/2\text{-}\pi$) was used, and the ^{31}P shifts were referenced to 85% H_3PO_4 solution at 0 ppm. For ^{11}B NMR, a rotor-synchronized spin-echo sequence of 5.85–11.7 µs ($\pi/2\text{-}\pi$) was applied, and the ^{11}B shifts were referenced to solid $LiBH_4$ powder at -41 ppm. ^7Li, ^{11}B, and ^{31}P spin-lattice relaxation time constants (T_1) were obtained by fitting on the spectra collected using an inversion recovery pulse ($\pi\text{-}\tau\text{-}\pi/2$) with a for ^7Li, ^{11}B, and ^{31}P, respectively. The variable-temperature T_1 measurements were conducted on a 300 MHz spectrometer. The Larmor frequencies are 116.6, 96.3, 121.4, and 300 MHz for ^7Li, ^{11}B, ^{31}P, and ^1H.

X-Ray Diffraction: High-resolution synchrotron powder diffraction data were collected using beamline 11-BM at the Advanced Photon Source (APS), Argonne National Laboratory, using an average wavelength of 0.458106 Å. Data points were collected at every 0.001° (2θ) with a scan speed of 0.01° s^{-1}. A mixture of NIST standard reference materials, Si (SRM 640c) and Al_2O_3 (SRM 676), was used to calibrate the instrument.

Neutron Diffraction: Room-temperature neutron total scattering experiments on the $(100\text{-}x)(0.75Li_2S\cdot0.25P_2S_5)\cdot xLiBD_4$ ($x = 40, 50,$ and 55) samples were performed at the Spallation Neutron Source at Oak Ridge National Laboratory (ORNL) at the NOMAD beamline (BL-1B). Around 0.5 g power for each compound was sealed inside vanadium containers in an argon-filled glovebox. The data acquisition took 6 hours for each sample. Then, background subtraction, flux normalization, and Placzek corrections were applied to the acquired data to generate the total scattering structural factor S(Q). Using the IDL codes,[44] the $S(Q)$ was Fourier transformed to the $G(r)$ within a Q range of 0.3 to 20 Å^{-1}.

Ionic Conductivity Measurements: Ionic conductivity was measured via impedance spectroscopy using a Biologic SP300 potentiostat/FRA. Ap-

proximately 350 mg of powder was pelletized under 300 MPa pressure in a custom pellet pressing hardware. A stack pressure of 8 MPa was applied during subsequent impedance measurements. Impedance spectra were collected from 7 MHz to 1 Hz with an AC amplitude of 100 mV. Ionic conductivity is determined from the measured resistance of the pellet and the pellet dimensions.

Scanning Electron Microscopy: The SEM images were acquired for the morphological analysis of $(100\text{-}x)$ $(0.75Li_2S\cdot0.25P_2S_5)\cdot xLiBD_4$ ($x = 40, 50,$ and 55). The samples were pressed into pellets, and SEM images of the sample surfaces were acquired on a NOVA NanoSEM 400 field-emission scanning electron microscope under 10 kV accelerating voltage.

First-Principle Calculations: Density functional theory (DFT) calculations were conducted to determine nuclear magnetic resonance (NMR) shielding tensors with the Vienna ab initio simulation package (VASP) using the projector augmented wave (PAW) method.[45,46] The Perdew-Burke-Ernzerhof generalized-gradient approximation (GGA-PBE) was employed as the exchange-correlation functional, along with PAW potentials integrated within VASP.[47] To generate representative structures for compounds $Li_{5-x}PS_4(BH_4)_{2-x}$, ordering function in Python Materials Genomics (pymatgen) package[48] was applied to select the first 25 configurations with the lowest electrostatic energies where Li ions and BH_4 units were randomly removed to create vacancies and meet the target stoichiometry based on experimentally refined argyrodite structures (unit cell expanded by $2 \times 1 \times 1$). These structures were further optimized with a plane-wave cutoff energy of 520 eV and a k-point sampling scheme of $1 \times 2 \times 2$. The unit cell parameters were allowed to relax during the structural optimization process to reflect the actual local structure instead of the average structure from the diffraction data. The AIMD simulations were performed using a canonical ensemble, with a time step of 2 fs, and processed according to Wang et al.'s work.[49] The simulations were initiated at a temperature of 100 K and then elevated to the target temperature linearly over a duration of 100 ps. The computation of chemical shifts was carried out using the linear response method developed by Yates et al.[50] Each computational spectrum contains results from at least 10 configurations to ensure sufficient sampling. Lorentzian broadening was applied to simulate the line broadening of experimental NMR spectra.

All-Solid-State Battery: The ASSBs were built using a Swagelok setup inside an argon-filled glovebox. The composite cathodes/catholytes were prepared by mixing NMC622, $(100\text{-}x)$ $(0.75Li_2S\cdot0.25P_2S_5)\cdot xLiBH_4$ ($x = 55$)/Li_6PS_5Cl, and vapor grown carbon nanofibers (VGCF) (67:30.5:2.5, wt%) in a mortar with pestle. First, the separator was made by compressing the $Li_{10}P_3S_{12}I$ solid electrolyte powder, which was synthesized according to the procedure described in the previous work.[51] Then, around 0.05 g composite cathodes were applied and compressed onto the separator. Li metal chips were used as the anodes. A stacking pressure of around 10 MPa and a charge/discharge current of 18.0 mAh g^{-1} (NMC) (0.09 C) were applied to the cells for the cycle life test with a voltage cutoff of [2.5 V, 4.3 V]. 30-s DC pulses were applied during the cell cycling to measure the cell resistance. The voltage and current before and after the 30-s pulses were used to calculate the resistance according to the equation: $R = \frac{V_1 - V_2}{I_1 - I_2}$.

Supporting Information

Supporting Information is available from the Wiley Online Library or from the author.

Conflict of Interest

The authors declare no conflict of interest.

Data Availability Statement

The data that support the findings of this study are available in the Supporting Information of this article.

Keywords

correlated motion, dual motor, neutron diffraction, polyanion rotation, solid-state NMR, superionic conductor

[1] Y. Li, S. Song, H. Kim, K. Nomoto, H. Kim, X. Sun, S. Hori, K. Suzuki, N. Matsui, M. Hirayama, T. Mizoguchi, T. Saito, T. Kamiyama, R. Kanno, *Science* **2023**, *381*, 50.

[2] L. Zhou, N. Minafra, W. G. Zeier, L. F. Nazar, *Acc. Chem. Res.* **2021**, *54*, 2717.

[3] P. Wang, S. Patel, J. E. Roberts, B. E. Francisco, Y.-Y. Hu, *ACS Mater. Lett.* **2024**, *6*, 2059.

[4] F. Strauss, S. Wang, C.-W. Nan, T. Brezesinski, *Matter* **2024**, *7*, 742.

[5] J. Lin, M. Schaller, G. Cherkashinin, S. Indris, J. Du, C. Ritter, A. Kondrakov, J. Janek, T. Brezesinski, F. Strauss, *Small* **2024**, *20*, 2306832.

[6] S. Li, J. Lin, M. Schaller, S. Indris, X. Zhang, T. Brezesinski, C. Nan, S. Wang, F. Strauss, *Angew. Chem., Int. Ed.* **2023**, *62*, e202314155.

[7] S. V. Patel, S. Banerjee, H. Liu, P. Wang, P.-H. Chien, X. Feng, J. Liu, S. P. Ong, Y.-Y. Hu, *Chem. Mater.* **2021**, *33*, 1435.

[8] P. Wang, H. Liu, S. Patel, X. Feng, P.-H. Chien, Y. Wang, Y.-Y. Hu, *Chem. Mater.* **2020**, *32*, 3833.

[9] X. Feng, P.-H. Chien, Y. Wang, S. Patel, P. Wang, H. Liu, M. Immediato-Scuotto, Y.-Y. Hu, *Energy Storage Mater.* **2020**, *30*, 67.

[10] P. Wang, S. Patel, H. Liu, P. Chien, X. Feng, L. Gao, B. Chen, J. Liu, Y. Hu, *Adv. Funct. Mater.* **2023**, *33*, 2307954.

[11] M. A. Kraft, S. Ohno, T. Zinkevich, R. Koerver, S. P. Culver, T. Fuchs, A. Senyshyn, S. Indris, B. J. Morgan, W. G. Zeier, *J. Am. Chem. Soc.* **2018**, *140*, 16330.

[12] S. Ohno, B. Helm, T. Fuchs, G. Dewald, M. A. Kraft, S. P. Culver, A. Senyshyn, W. G. Zeier, *Chem. Mater.* **2019**, *31*, 4936.

[13] Y. B. Song, D. H. Kim, H. Kwak, D. Han, S. Kang, J. H. Lee, S.-M. Bak, K.-W. Nam, H.-W. Lee, Y. S. Jung, *Nano Lett.* **2020**, *20*, 4337.

[14] F. Zhao, J. Liang, C. Yu, Q. Sun, X. Li, K. Adair, C. Wang, Y. Zhao, S. Zhang, W. Li, S. Deng, R. Li, Y. Huang, H. Huang, L. Zhang, S. Zhao, S. Lu, X. Sun, *Adv. Energy Mater.* **2020**, *10*, 1903422.

[15] L. Zhou, A. Assoud, Q. Zhang, X. Wu, L. F. Nazar, *J. Am. Chem. Soc.* **2019**, *141*, 19002.

[16] I. Hanghofer, B. Gadermaier, H. M. R. Wilkening, *Chem. Mater.* **2019**, *31*, 4591.

[17] H. Fang, P. Jena, *Proc. Natl. Acad. Sci. USA* **2017**, *114*, 11046.

[18] R. Aronsson, H. E. Gunilla Knape, A. Lundén, L. Nilsson, L. M. Torell, N. Hessel, Andersen, J. K. Kjems, *Radiat. Eff. Defects Solids* **1983**, *75*, 79.

[19] Z. Zhang, L. F. Nazar, *Nat. Rev. Mater.* **2022**, *7*, 389.

[20] P. Tsai, S. Mair, J. Smith, D. M. Halat, P. Chien, K. Kim, D. Zhang, Y. Li, L. Yin, J. Liu, S. H. Lapidus, J. A. Reimer, N. P. Balsara, D. J. Siegel, Y. Chiang, *Adv. Energy Mater.* **2023**, *13*, 2203284.

[21] Y. Jang, H. Seo, Y. Lee, S. Kang, W. Cho, Y. W. Cho, J. Kim, *Adv. Sci.* **2023**, *10*, 2204942.

[22] Y. Sun, B. Ouyang, Y. Wang, Y. Zhang, S. Sun, Z. Cai, V. Lacivita, Y. Guo, G. Ceder, *Matter* **2022**, *5*, 4379.

[23] M. Matsuo, Y. Nakamori, S. Orimo, H. Maekawa, H. Takamura, *Appl. Phys. Lett.* **2007**, *91*, 224103.

[24] H. Maekawa, M. Matsuo, H. Takamura, M. Ando, Y. Noda, T. Karahashi, S. Orimo, *J. Am. Chem. Soc.* **2009**, *131*, 894.

[25] A. El Kharbachi, Y. Hu, K. Yoshida, P. Vajeeston, S. Kim, M. H. Sørby, S. Orimo, H. Fjellvåg, B. C. Hauback, *Electrochim. Acta* **2018**, *278*, 332.

[26] A. Sakuda, A. Yamauchi, S. Yubuchi, N. Kitamura, Y. Idemoto, A. Hayashi, M. Tatsumisago, *ACS Omega* **2018**, *3*, 5453.

[27] Y. Sun, Y. Wang, X. Liang, Y. Xia, L. Peng, H. Jia, H. Li, L. Bai, J. Feng, H. Jiang, J. Xie, *J. Am. Chem. Soc.* **2019**, *141*, 5640.

[28] A. Unemoto, H. Wu, T. J. Udovic, M. Matsuo, T. Ikeshoji, S. Orimo, *Chem. Commun.* **2016**, *52*, 564.

[29] M. Matsuo, A. Remhof, P. Martelli, R. Caputo, M. Ernst, Y. Miura, T. Sato, H. Oguchi, H. Maekawa, H. Takamura, A. Borgschulte, A. Züttel, S. Orimo, *J. Am. Chem. Soc.* **2009**, *131*, 16389.

[30] A. Yamauchi, A. Sakuda, A. Hayashi, M. Tatsumisago, *J. Power Sources* **2013**, *244*, 707.

[31] A. Unemoto, M. Matsuo, S. Orimo, *Adv. Funct. Mater.* **2014**, *24*, 2267.

[32] M. Matsuo, S. Orimo, *Adv. Energy Mater.* **2011**, *1*, 161.

[33] T. K. Schwietert, A. Vasileiadis, M. Wagemaker, *JACS Au* **2021**, *1*, 1488.

[34] K. Kisu, S. Kim, H. Oguchi, N. Toyama, S. Orimo, *J. Power Sources* **2019**, *436*, 226821.

[35] H. Fang, P. Jena, *Nat. Commun.* **2022**, *13*, 2078.

[36] J. G. Smith, D. J. Siegel, *Nat. Commun.* **2020**, *11*, 1483.

[37] A. Lee, S. Sarker, J. E. Saal, L. Ward, C. Borg, A. Mehta, C. Wolverton, *Commun. Mater.* **2022**, *3*, 73.

[38] R. Gautier, X. Zhang, L. Hu, L. Yu, Y. Lin, T. O. L. Sunde, D. Chon, K. R. Poeppelmeier, A. Zunger, *Nat. Chem.* **2015**, *7*, 308.

[39] H. Zhu, G. Hautier, U. Aydemir, Z. M. Gibbs, G. Li, S. Bajaj, J.-H. Pöhls, D. Broberg, W. Chen, A. Jain, M. A. White, M. Asta, G. J. Snyder, K. Persson, G. Ceder, *J. Mater. Chem. C* **2015**, *3*, 10554.

[40] Y. Zeng, B. Ouyang, J. Liu, Y.-W. Byeon, Z. Cai, L. J. Miara, Y. Wang, G. Ceder, *Science* **2022**, *378*, 1320.

[41] J. Zheng, M. Tang, Y.-Y. Hu, *Angew. Chem.* **2016**, *128*, 12726.

[42] F. Marchini, B. Porcheron, G. Rousse, L. Albero Blanquer, L. Droguet, D. Foix, T. Koç, M. Deschamps, J. M. Tarascon, *Adv. Energy Mater.* **2021**, *11*, 2101111.

[43] V. Domenici, *Phys. Chem. Chem. Phys.* **2009**, *11*, 8496.

[44] J. Neuefeind, M. Feygenson, J. Carruth, R. Hoffmann, K. K. Chipley, *Nucl. Instrum. Methods Phys. Res., Sect. B* **2012**, *287*, 68.

[45] P. E. Blöchl, *Phys. Rev. B* **1994**, *50*, 17953.

[46] G. Kresse, J. Furthmüller, *Phys. Rev. B* **1996**, *54*, 11169.

[47] J. P. Perdew, K. Burke, M. Ernzerhof, *Phys. Rev. Lett.* **1996**, *77*, 3865.

[48] S. P. Ong, W. D. Richards, A. Jain, G. Hautier, M. Kocher, S. Cholia, D. Gunter, V. L. Chevrier, K. A. Persson, G. Ceder, *Comput. Mater. Sci.* **2013**, *68*, 314.

[49] Y. Wang, W. D. Richards, S. P. Ong, L. J. Miara, J. C. Kim, Y. Mo, G. Ceder, *Nat. Mater.* **2015**, *14*, 1026.

[50] J. R. Yates, C. J. Pickard, F. Mauri, *Phys. Rev. B* **2007**, *76*, 024401.

[51] X. Feng, P.-H. Chien, S. Patel, J. Zheng, M. Immediato-Scuotto, Y. Xin, I. Hung, Z. Gan, Y.-Y. Hu, *Energy Storage Mater.* **2019**, *22*, 397.